

Received 1 April 2005  
Accepted 7 September 2005

# Time-of-flight neutron transmission of mosaic crystals

Javier R. Santisteban

ISIS Facility, Rutherford Appleton Laboratory, Chilton, Didcot, OX11 0QX, UK. Correspondence e-mail: j.r.santisteban@rl.ac.uk

The energy-dispersive neutron transmission of mosaic crystals presents a series of dips in intensity as a result of reflection in the crystal planes. The positions of these dips can be exploited for the definition of the crystal orientation with a resolution of 1 min of arc. The widths of these dips depend on crystal orientation, on the reflection index, on the mosaicity, and on the incident-beam divergence. The capability of the technique to define the orientation and mosaicity of a Cu crystal has been assessed through time-of-flight experiments. A Cu monochromator has been plastically deformed by uniaxial tension *in situ*, and the evolution of crystal orientation and mosaicity was tracked using the technique. Several crystal reflections at different locations of the sample were simultaneously studied during the experiment. A linear increase of mosaicity on deformation at an average rate of ~5 min per percentage of shear strain was observed. The reorientation of the crystal as a result of the applied load showed variations across the specimen.

© 2005 International Union of Crystallography  
Printed in Great Britain – all rights reserved

## 1. Introduction

Monocrystals are used in neutron spectrometers as monochromators to select specific neutron wavelengths. The monocrystals used as monochromators consist of slightly misaligned smaller blocks. The mosaic spread or mosaicity of the crystal is a measure of this misalignment. The diffracted intensity from a neutron monochromator is roughly proportional to its mosaicity. Monochromators are usually required to display an anisotropic mosaic spread, with the mosaicity in the diffraction plane matching the incident-beam divergence, whilst normal to this plane the mosaicity is kept low for efficient focusing of the beam on the sample. However, crystals are grown rather perfectly, with mosaicities of a few minutes of

arc, making them useless as neutron monochromators. Consequently, several methods have been proposed to increase the mosaic spread of perfect crystals through elastic bending or plastic deformation (Frey, 1974). The production of mosaic crystals with a controlled and homogeneous mosaicity by plastic deformation is not an easy task, and so far the process is quite inefficient in both time and material; a large proportion of the crystals are unusable at the end of the production stage and a significant amount of time is spent in testing and characterization (Courtois *et al.*, 2002).

Besides this practical interest, the plastic deformation of monocrystals is of great interest *per se* as these studies may reveal basic phenomena of deformation processes. As an example, the formation of deformation bands in face-centred cubic (f.c.c.) crystals strained in tension along the [110] direction has recently received a renewed interest in the literature (Kashihara *et al.*, 1996; Wert & Huang, 2003; Wert, 2004).

We introduce a new experimental technique capable of monitoring the variation in orientation, mosaicity, lattice parameters and interplanar distances in mosaic crystals deformed *in situ* based on a spectroscopic analysis of the transmitted neutrons. The technique is simple: the sample is placed in the neutron beam and a detector is located just behind the sample, as shown schematically in Fig. 1(a). The transmission method essentially compares the

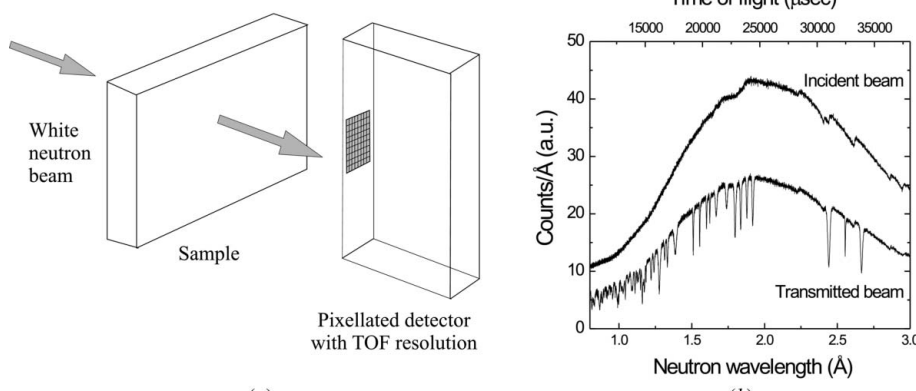


**Figure 1**

(a) Experimental arrangement for neutron transmission. (b) Typical time-of-flight neutron spectra for a direct beam (top), and for a neutron beam transmitted along the [110] direction of a 10 mm-thick Cu monochromator (bottom).

reduction in intensity brought about by the insertion of a sample, as is exemplified in Fig. 1(b) for a Cu mosaic crystal. In the transmitted beam, neutrons that have interacted with the sample are missing. It is therefore possible to derive crystallographic information about the sample by analysing this transmitted spectrum. Several spectra are usually recorded at different specimen orientations, in order to extract information from the changes that appear in the transmitted intensity (Santisteban, Steuwer *et al.*, 2002). For transmission experiments performed at pulsed sources, neutrons produced in short pulses have their wavelength determined by their time-of-flight (TOF) along a fixed flight path. Moreover, by using a pixellated array of detectors that records the spatial variation of the transmission across the sample, it is possible to produce TOF ‘radiographs’ in specimens having dimensions of centimetres.

## 2. Neutron transmission of mosaic crystals

Fig. 1(b) exemplifies the reduction of intensity brought about by the insertion of a mosaic crystal in a polychromatic neutron beam. The complex dependence of the attenuation on neutron wavelength can be explained by identifying all the processes removing neutrons from the beam. Each neutron incident on the crystal is either Bragg reflected ( $R$ ), scattered ( $S$ ), absorbed ( $A$ ), or transmitted ( $T$ ), so that  $R + S + A + T = 1$ . The transmission is given by  $T = I/I_0$ , where  $I$  and  $I_0$  are the beam intensities recorded with and without sample, respectively. The transmission in TOF,  $t$ , is converted into a neutron wavelength  $\lambda$  scale via

$$\lambda = \frac{h}{mL}(t - t_0) \quad (1)$$

with  $h$  Planck’s constant,  $m$  the neutron mass,  $L$  the total flight path and  $t_0$  an instrumental delay time. The values of  $L$  and  $t_0$  are obtained by measuring the transmission of a reference powder sample (Santisteban *et al.*, 2001).

The three processes removing neutrons from the incident beam have been identified in Fig. 2, which shows the transmission for a Cu monochromator. To help the interpretation and subsequent analysis, the experimental data are presented in terms of the complement of the transmission, *i.e.*  $(1 - T) = R + S + A$ . As seen from the figure, the overall reduction of beam intensity is governed by nuclear absorption and thermal diffuse scattering. Neutron absorption is independent of the temperature and presents a linear dependence that becomes dominant at long wavelengths, whilst thermal diffuse scattering dominates at short wavelengths and is temperature-dependent. Theoretical expressions to calculate the thermal diffuse scattering have been given by Freund (1983) and Granada (1984). The theoretical curves in Fig. 2 were calculated using the latter.

On the other hand, Bragg reflected neutrons result in sharp peaks at precise wavelengths specified by Bragg’s law,

$$\lambda_{hkl} = 2d_{hkl} \sin \theta_B, \quad (2)$$

where  $d_{hkl}$  is the interplanar distance for the  $(hkl)$  plane and  $\theta_B$  is the Bragg angle. These peaks are just an indirect manifestation in the transmitted beam of the spots recorded on traditional Laue photographs. Sears (1997) has comprehensively discussed the phenomenon of Bragg reflection in mosaic crystals, providing general expressions for the diffracted intensity for both Bragg and Laue geometries. Alianelli (2002) has discussed the calculation of the reflectivity of real monochromators by incorporating such expressions within Monte Carlo computer codes. Naguib & Adib (1996) have described a computer code that calculates the transmission of mosaic crystals *versus* neutron wavelength. We study the transmission of mosaic crystals by TOF experiments, and concentrate on the analysis of the position and width of the Bragg-reflected peaks as a tool for the study of the plastic deformation of mosaic crystals.

## 3. Experiment

The transmission experiments were performed on the ENGIN-X instrument (Dann *et al.*, 2004), a TOF neutron diffractometer optimized for engineering measurements at the ISIS Facility, Rutherford Laboratory, UK. The only features of the instrument relevant to these transmission experiments are the incident beam and the detector system.

### 3.1. Incident beam

ENGIN-X has a polychromatic incident beam, with the wavelength distribution shown in Fig. 1(b). In ENGIN-X, a pulsed neutron beam produced in a methane moderator travels along a supermirror guide ( $m = 3$ ) up to the sample position 50 m away from the moderator. The guide is curved from 4 m to 37 m, and straight between 37 m and 48.5 m. Two sets of counter-rotating choppers located at 6 m and 9 m allow a flexible definition of the wavelength window (0.5–10 Å) and

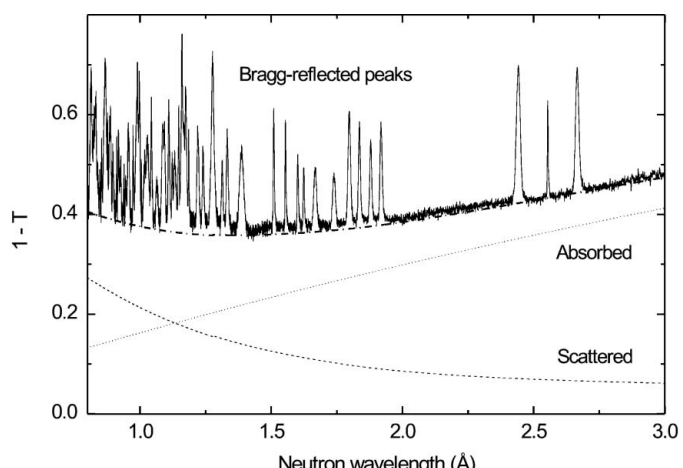


**Figure 2**

Contributions to the attenuation of a neutron beam in a mosaic crystal. The solid line represents the experimental data for a Cu crystal along the [110] direction. The peaks appear from reflection in the crystal planes. The dotted and dashed lines are the nuclear absorption and thermal diffuse scattering, respectively. The dashed-dotted line is the sum of both contributions.

**Table 1**

Typical parameters of the peaks observed in  $(1 - T)$ , measured along the [110] direction of the reference Cu sample.

Index $hkl$	Experimental position $\lambda_{hkl}^{\text{exp}}$ (Å)	Fit position $\lambda_{hkl}^{\text{fit}}$ (Å)	Difference $\lambda_{hkl}^{\text{exp}} - \lambda_{hkl}^{\text{fit}}$ ( $\mu\text{\AA}$ )	Gauss width $\delta\sigma_{hkl}$ ( $\mu\text{\AA}$ )	Angle $\alpha_{hkl}$ (°)
[111]	3.4366 (1)	3.43629	98	1890 (40)	34.546 (2)
[111]	3.3676 (1)	3.36835	-224	1970 (30)	36.184 (2)
[020]	2.6760 (1)	2.6760	-16	1970 (50)	42.219 (3)
[220]	2.55210 (3)	2.55174	142	260 (10)	2.74 (1)
[200]	2.4268 (1)	2.42748	-267	2260 (50)	47.807 (2)
[131]	1.91014 (5)	1.91026	-59	1080 (30)	28.760 (3)
[131]	1.89170 (5)	1.89173	-18	1280 (30)	29.752 (2)
[311]	1.81968 (5)	1.81989	-113	1280 (40)	33.371 (3)
[311]	1.80126 (5)	1.80136	-55	1200 (40)	34.241 (2)
[222]	1.71788 (6)	1.71814	-150	1660 (40)	34.567 (3)
[222]	1.68402 (6)	1.68418	-92	1800 (50)	36.173 (3)
[331]	1.61699 (4)	1.61699	0	520 (40)	12.757 (6)
[331]	1.60621 (4)	1.60626	-32	550 (30)	14.347 (5)
[240]	1.55581 (4)	1.55589	-55	380 (30)	15.679 (5)
[420]	1.50625 (4)	1.50619	36	620 (30)	21.232 (4)

the frequency of operation (5–50 Hz). The lowest wavelength achievable ( $\sim 0.5$  Å) is defined by the curvature of the incident neutron guide (5 km). Two pairs of slits inserted in the final straight part of the guide (Slit 1 at 46 m and Slit 2 at 48.5 m) allow the incident angular resolution to be modified. The beam cross section is defined with a pair of motorized slits (Slit 3) that moves between the end of the guide and the sample position.

### 3.2. Detector

The detector is aligned with the incident beam and records the neutrons as a function of their TOF. We use a pixellated detector bank consisting of a  $10 \times 10$  array of  $2 \times 2$  mm scintillation detectors on a 2.5 mm pitch (Santisteban, Edwards *et al.*, 2002). The detectors are coupled *via* fibre optic light guides to position-sensitive photo-multiplier tubes. Signals from the photo-multiplier tubes are amplified by preamplifiers in the detector housing and then transferred *via* cables to remote amplifier/pulse height discriminator electronics. The digital outputs from each pixel are stored in a histogram memory for subsequent analysis. A TOF spectrum similar to those shown in Fig. 1(b) is produced for each pixel. For experiments not requiring spatial resolution the pixels are summed for a faster count rate.

### 3.3. Data reduction

We have performed test experiments on a reference specimen, a plate with dimension of  $30 \times 30 \times 8$  mm, with the [110] crystallographic direction along the normal direction, produced by the Optics Laboratory of the Institut Laue Langevin, France. The positions, widths and intensities of the well resolved peaks of the spectrum are defined by least-squares refinement using an analytic peak profile. Although not obvious from Fig. 2, the peak shape is asymmetric, a characteristic of TOF instruments resulting from the convolution of the moderator and geometric contributions to the resolution (Ikeda & Carpenter, 1985). We used a relatively simple peak profile, *i.e.* the convolution of a truncated decaying exponential for the moderator broadening with a

Gaussian distribution accounting for geometric and sample-induced broadening (Kropff *et al.*, 1982). The instrument and sample contributions are easily deconvolved with this line shape, thus simplifying the quantification and interpretation of the observed peak broadening.

The least-squares fits were performed keeping fixed the parameter  $\tau$  describing the exponential decay, *i.e.* the moderator contribution to the peak width. We have found this fitting constraint to be imperative in order to obtain reliable values of peak positions and widths. The dependence of  $\tau$  on neutron wavelength was measured by conventional diffraction experiments on a reference CeO<sub>2</sub> powder using ENGIN-X diffraction banks.

The least-squares refinements performed through this work were excellent for most reflections. Table 1 lists typical results for the peak parameters resulting from the least-squares refinement from a single transmission spectrum, together with calculated peak positions and angles as explained in the following section. The results correspond to the transmission along a direction very close to the [110] direction. In order to compare the width of peaks centred at different wavelengths, relative peak widths are used through this paper, *i.e.*

$$\delta\sigma_{hkl} = \frac{\sigma_{hkl}}{t_{hkl}} \times 10^6, \quad (3)$$

where  $\sigma_{hkl}$  and  $t_{hkl}$  are the Gaussian width and peak position, respectively. Table 1 lists the relative peak widths expressed (unitless) in  $\mu\text{\AA}$  ( $1 \mu\text{\AA} = 10^{-6}$ ), the standard unit in elastic strain analysis.

## 4. Peak positions and crystal orientation

### 4.1. Directions cosines

The positions of the diffraction peaks depend on the orientation between the incident beam and the crystal. For a cubic crystal with lattice parameter  $a$ , the  $[hkl]$  reflection diffracts neutrons of wavelength

$$\lambda_{hkl} = 2a \frac{|ha_{11} + ka_{12} + la_{13}|}{h^2 + k^2 + l^2}, \quad (4)$$

where  $a_{11}$ ,  $a_{12}$  and  $a_{13}$  are the direction cosines of the incident neutron beam in the coordinate system of the crystal. An alternative expression of Bragg's law, useful for the interpretation of the transmitted spectrum, is

$$\lambda_{hkl} = 2d_{hkl} \cos \alpha_{hkl}, \quad (5)$$

where  $d_{hkl}$  is the distance between the planes perpendicular to the  $[hkl]$  direction, and  $\alpha_{hkl}$  is the angle between  $[hkl]$  and the neutron beam. Hence, the peaks appearing in Fig. 2 correspond to the projections of all interplanar distances  $d_{hkl}$  along the direction of the incident neutron beam. A method for indexing these peaks, which exploits the existence of a cut-off wavelength at  $\lambda_{hkl}^{\max} = 2d_{hkl}$  for each crystal family, is explained in Appendix A. After a reflection has been indexed, the angle  $\alpha_{hkl}$  can be precisely calculated from the peak position  $\lambda_{hkl}$  using equation (5). Values of  $\alpha_{hkl}$  are listed in Table 1.

Since a single transmission spectrum accesses many reflections, the peak positions can be exploited for a precise determination of the crystal orientation. As equation (4) suggests, this can be easily achieved by a multi-linear regression on the observed peak positions  $\lambda_{hkl}$  using

$$\begin{aligned} x_1 &= h \left( \frac{2a}{h^2 + k^2 + l^2} \right), \\ x_2 &= k \left( \frac{2a}{h^2 + k^2 + l^2} \right), \\ x_3 &= l \left( \frac{2a}{h^2 + k^2 + l^2} \right), \end{aligned} \quad (6)$$

as independent variables, and the direction cosines  $a_{11}$ ,  $a_{12}$  and  $a_{13}$ , as fitting parameters. Strictly speaking, only two direction cosines are independent, as they are related by the normalization condition

$$a_{11}^2 + a_{12}^2 + a_{13}^2 = 1. \quad (7)$$

However, for simplicity and numerical stability it is better to consider them as independent variables during the least-squares refinement and perform the normalization afterwards. In doing so, the normalization factor provides a precise determination of the actual lattice parameter of the crystal.

The very good agreement between the experimental and calculated peak positions, as given by the difference column in Table 1, indicates the efficiency of this approach. The standard deviation between the experimental and calculated peak positions is  $90 \mu\text{e}$ . The refined value for the lattice parameter is  $a = 3.61334(4) \text{ \AA}$ . The refined values for the direction cosines are  $a_{11} = 0.01737(2)$ ,  $a_{12} = 0.73830(1)$  and  $a_{13} = 0.67424(1)$ . In all cases the referred uncertainties correspond to the uncertainty estimated from the least-squares refinement process. Possible systematic errors due to the existence of elastic strains inside the sample are discussed later.

## 4.2. Orientation matrix

The directions cosines determined in the previous section give the coordinates of the incident-beam direction in the coordinate system of the crystal. In order to define the complete transformation matrix between the laboratory and crystal systems, we need to provide the direction cosines of at least two laboratory directions,  $\mathbf{v}_1$  and  $\mathbf{v}_2$ , in the coordinate system of the crystal. We assume that  $\mathbf{v}_1$  and  $\mathbf{v}_2$  define the  $XY$  plane of the laboratory system, and set the  $X$  axis along  $\mathbf{v}_1$ . Then, the direction cosines of the laboratory  $Y$  and  $Z$  axes in the coordinate system of the crystal are simply given by the vector products

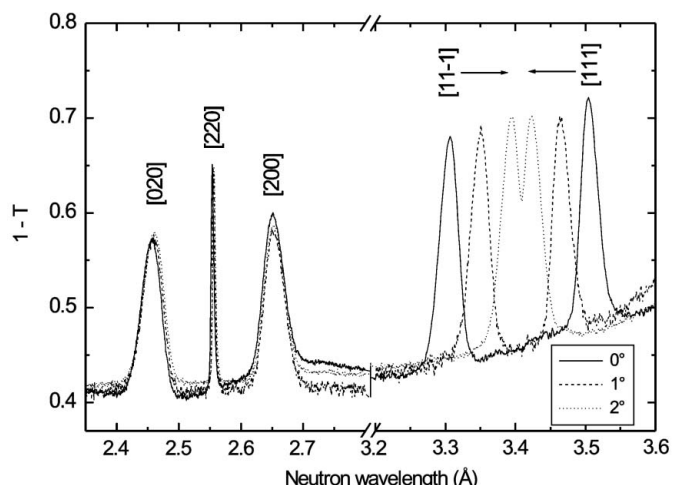
$$\hat{\mathbf{x}} = \mathbf{v}_1 = (a_{11}, a_{12}, a_{13}), \quad (8a)$$

$$\hat{\mathbf{z}} = \mathbf{v}_1 \times \mathbf{v}_2 = (a_{31}, a_{32}, a_{33}), \quad (8b)$$

$$\hat{\mathbf{y}} = \hat{\mathbf{z}} \times \mathbf{v}_1 = (a_{21}, a_{22}, a_{23}), \quad (8c)$$

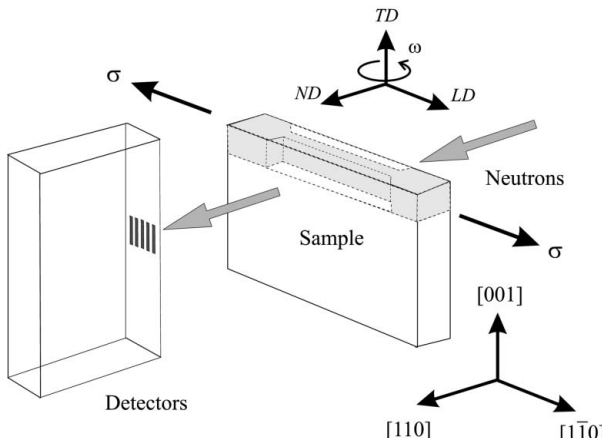
which implicitly define  $a_{ij}$ , the transformation matrix between crystal and laboratory coordinate systems (Bunge, 1982). In most cases, however, we are actually interested in the transformation matrix between the crystal coordinate system and the macroscopic coordinate system of the specimen (normal, transverse and longitudinal directions: LD, TD, ND). That transformation is easily obtained from the transformation matrix between the laboratory and the specimen coordinates systems, defined by optical means during the alignment of the specimen in the neutron beam.

In practice, the two directions  $\mathbf{v}_1$  and  $\mathbf{v}_2$  are obtained by defining the direction cosines of the incident beam at two sample orientations, separated by a rotation around the laboratory  $Z$  axis. Fig. 3 shows a detail of the changes appearing in the transmission spectrum of a Cu monochromator as the specimen is rotated in this way. Fig. 4 displays the shape ( $10 \times 50 \times 100 \text{ mm}$ ) and crystal orientation of the specimen. In this experiment the crystal was rotated around LD, and transmission spectra were recorded at



**Figure 3**

Shifts in peak position as a result of rotation of the specimen. At  $0^\circ$ , the incident beam was aligned with the  $[110]$  direction. The rotation was performed around the  $[110]$  direction.

**Figure 4**

Geometry and orientation of the monochromator studied in this work, showing the experimental arrangement used for the tensile loading tests. Five locations of the sample are measured simultaneously, as defined by the five detectors indicated in the figure.

selected orientations. The figure clearly shows that the associated peaks shifts, and hence the crystal orientation, are easily resolved by the TOF transmission technique. The transmitted spectra were produced by adding together 32 pixels in the detection bank, which corresponds to a sampling area of  $10 \times 20$  mm on the specimen. This allows using counting times of only 150 s per orientation. The spectrum labelled  $0^\circ$  corresponds to an orientation in which ND was aligned with the incident beam and LD was along the vertical ( $Z$ ) axis of the laboratory. At  $2^\circ$  from this initial orientation peaks from the  $[111]$  and  $[1\bar{1}\bar{1}]$  reflections appear overlapped, which could hamper the refinement of the individual peak locations. The phenomenon of having two or more reflections satisfying Bragg condition for nearly the same wavelength has been called ‘parasitic scattering’ due to its detrimental effect in the production of monochromatic neutron beams (O’Connor & Sosnowski, 1961). As the graphic shows, however, the crystals can always be easily ‘tuned’, *i.e.* oriented at a very precise angle, so that all reflections of interest are effectively separated. The graph also suggests that two transmission spectra separated by an angle as small as  $1^\circ$  can be effectively used to determine the transformation matrix between laboratory and crystal systems. Rotating by just a small angle is advantageous as this minimizes the differences in the actual volume of the sample gauged by the neutron beam at each exposition.

By applying the method described above using the spectra recorded at  $0^\circ$  and  $1^\circ$ , we have found that the  $[001]$  and  $[1\bar{1}0]$  directions of the crystal were  $2.5^\circ$  off the transverse and longitudinal directions of the specimen. For this study, the direction cosines defining  $\mathbf{v}_1$  and  $\mathbf{v}_2$  were calculated from the refinement of the first six reflections.

## 5. Peak widths and mosaicity

The widths of the peaks listed in Table 1 vary strongly between reflections because of the instrument resolution dependence on neutron wavelength and diffraction angle. The latter effect is visually evident in Fig. 3, where reflections  $[200]$  and  $[020]$

are much wider than the  $[220]$  peak, even when all peaks appear at nearly the same wavelength. The resolution of a TOF instrument is defined by all the experimental errors contributing to the uncertainty in the TOF of the neutrons. This TOF can be separated in two parts:

$$t = t_m + t_L = t_m + \frac{mL\lambda}{h}, \quad (9)$$

where  $t_m$  is the emission time when the neutron leaves the moderator, and  $t_L$  is the time that the neutron spends traveling from the face of the moderator to the detector, and the other symbols have been defined in equation (1). In reality, experimental uncertainties mean that both  $t_m$  and  $t_L$  have associated probability distributions  $P_m(t_m)$  and  $P_L(t_L)$ , and the instrument resolution corresponds to the convolution of these distributions. We can estimate the width of the  $[hkl]$  reflection from

$$\left( \frac{\Delta t_{hkl}}{t_{hkl}} \right)^2 = \left( \frac{\Delta t_m}{t_{hkl}} \right)^2 + \left( \frac{\Delta L}{L} \right)^2 + \left( \frac{\Delta \lambda_{hkl}}{\lambda_{hkl}} \right)^2, \quad (10)$$

since  $t_m$  is small compared with  $t_L$ . Here  $\Delta t_m$ ,  $\Delta L$  and  $\Delta \lambda_{hkl}$  are the uncertainties in emission time, flight path and neutron wavelength, respectively. For ENGIN-X, the relative uncertainty in flight path is small ( $\Delta L/L \simeq 5 \times 10^{-5}$ ) and can be neglected. The moderator distribution  $P_m(t_m)$  is an asymmetric function with a width dependent on the neutron wavelength, which has been extensively discussed in the literature (Ikeda & Carpenter, 1985). As mentioned in §3.3, in our peak analysis  $P_m(t_m)$  has been represented by a truncated exponential with a decay constant  $\tau$ , so  $\Delta t_m$  is essentially proportional to  $\tau$ , which depends on neutron wavelength. The uncertainty in neutron wavelength  $\Delta \lambda_{hkl}$  comes from Bragg’s law. To see this, we note that a peak in  $(1 - T)$  represents all the neutrons that have been removed from the incident beam as a result of Bragg reflection on a particular crystal plane. For an ideally perfect crystal only neutrons of a single wavelength  $\lambda_{hkl}$  are removed from the beam, and the width of the peak corresponds to the moderator distribution  $P_m(t)$ . But in a mosaic crystal the Bragg condition is relaxed, as a finite distribution of crystal orientations and interplanar distances exist within the crystal. The dependence of  $(\Delta \lambda_{hkl})^2$  on the experimental parameters is found from Bragg’s law,

$$\left( \frac{\Delta \lambda_{hkl}}{\lambda_{hkl}} \right)^2 = \left( \frac{\Delta d_{hkl}}{d_{hkl}} \right)^2 + (\Delta \alpha_{hkl})^2 \tan^2 \alpha_{hkl}, \quad (11)$$

where we have assumed that there is no correlation between  $d_{hkl}$  and  $\alpha_{hkl}$ . The first term  $(\Delta d_{hkl}/d_{hkl})^2$  comes from the elastic deformation of the crystal lattice, whilst the second term  $(\Delta \alpha_{hkl})^2$  reflects the finite distribution of scattering angles. In the context of our least-squares refinement of the peaks,  $(\Delta \lambda_{hkl}/\lambda_{hkl})^2$  corresponds to the relative width  $\delta \sigma_{hkl}^2$  of the Gaussian contribution to the peak broadening.

Fig. 5 shows the relative peak widths  $\delta \sigma_{hkl}$  measured for the reference Cu mosaic crystal at different orientations for two experimental arrangements labelled 1 and 2. The solid symbols correspond to arrangement 1, a configuration where slits 1 and 2 are set to  $20 \times 20$  mm, and slit 3 is set to  $18 \times$

18 mm at 0.1 m from the sample. The open symbols correspond to arrangement 2, where slits 1 and 2 are set to 15 × 15 mm, and slit 3 is set to 11 × 11 mm at 0.08 m from the sample.

The solid symbols are the widths of all reflections between 1.7 Å and 2.3 Å at six different orientations, with the angle between ND and the incident beam between 60° and 70°. The area of the sample covered by experiment was a 7 × 7 mm square, as defined by the nine central pixels of the detector. The open symbols are the widths of all reflections between 1.5 Å and 2.7 Å from the transmission along ND. In this arrangement, transmission spectra were recorded at five positions in the sample, each one over an area of 9.5 × 2 mm. The data plotted in the figure correspond to the average peak widths measured across the specimen and the error bars are the associated standard deviations.

Equation (11) describes well the dependence of the Gaussian peak width on  $\tan \alpha_{hkl}$  in both cases. Least-squares fits to the data provide  $\Delta\alpha_{hkl}$  values of  $(2746 \pm 90) \mu\text{e}$  for the solid symbols and  $(1733 \pm 100) \mu\text{e}$  for the open symbols, and  $(\Delta d_{hkl}/d_{hkl})$  values of  $(180 \pm 100) \mu\text{e}$  and  $(280 \pm 150) \mu\text{e}$ , respectively. The small values of  $(\Delta d_{hkl}/d_{hkl})$  are expected for this sample, where most deformation is accommodated plastically, due to the low yield stress of Cu single crystals. On the other hand, the uncertainty  $\Delta\alpha_{hkl}$  in the Bragg diffraction angle, equivalent to 9.5 and 6 min of arc, respectively, arises from the misalignment of mosaic blocks as well as from the divergence of the incident beam.

The divergence of the incident beam  $\eta$  is defined by the neutron guide and the slit arrangement. We have studied the divergence in the two arrangements using the Monte Carlo code *MCStas* (Nielsen & Lefmann, 2000). We have calculated  $\eta^2$  as the second moment of the distribution describing the incident-beam intensity as a function of the incident-beam direction. The resulting values are 8.79 min for arrangement 1 and 5.71 min for arrangement 2, which correspond to  $2557 \mu\text{e}$  and  $1661 \mu\text{e}$ , respectively.

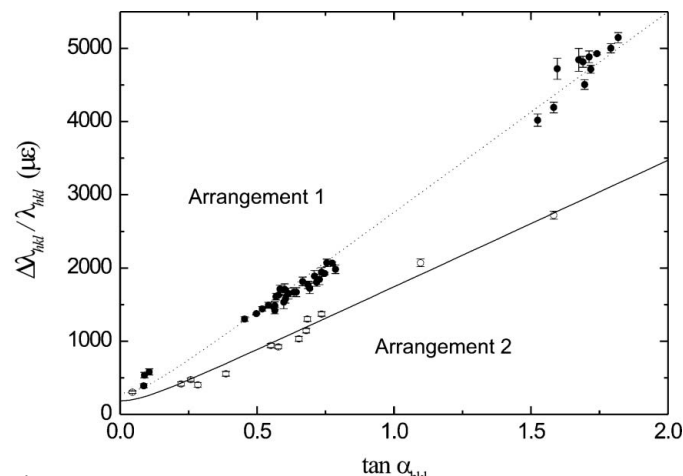


Figure 5

Dependence of peak width on the angle  $\alpha_{hkl}$  between the incident beam and  $[hkl]$ , the normal to the reflection plane, for a sample with a mosaicity of 3 min. The solid and open symbol are for incident-beam divergences of 10 min and 4.5 min, respectively.

On the other hand, the contribution from the finite distribution of crystal orientations is usually characterized by the crystal mosaicity. The mosaicity for the  $[hkl]$  reflection is measured by recording rocking curves  $W_{hkl}^n(\varphi)$ , where  $\varphi$  is the rocking angle around the sample direction  $\mathbf{n}$ , corresponding to the normal to the diffraction plane. The rocking curves measured using  $\gamma$ -rays reflect the intrinsic mosaicity of a specimen (Schneider, 1974), whilst neutrons provide a convolution of the intrinsic mosaicity with the resolution of the instrument. Fig. 6(a) shows schematically a standard mosaicity measurement using neutrons, where an orientation distribution  $W_{hkl}(\varphi, \psi)$  in the neighborhood of the direction  $[hkl]$  is studied with a monochromatic beam and a detector at a fixed angle. The angle  $\varphi$  represents rotations in the diffraction plane, whilst  $\psi$  represents rotations normal to it. The experimental arrangement defines the scattering vector  $\mathbf{q}$  with a resolution determined by the collimation in the incident and diffracted beams, as schematically represented by the white rectangle near the tip of  $\mathbf{q}$ . As the specimen is rocked around

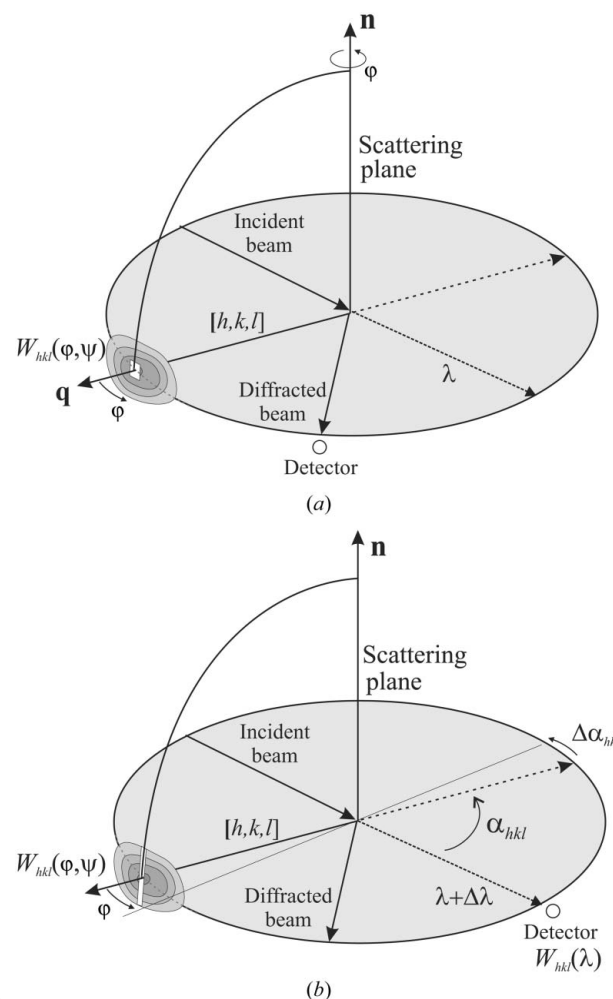


Figure 6

Schematic diagram explaining the peak widths measured for (a) a rocking curve on a constant-wavelength experiment and (b) a TOF transmission experiment. The distribution  $W_{hkl}(\varphi, \psi)$  gives the number of crystals misaligned by  $(\varphi, \psi)$  from the average crystal orientation. The angles  $\varphi$  and  $\psi$  are the misalignments in and out of the diffraction plane, respectively.

the diffraction plane normal  $\mathbf{n}$ , the intensity  $W_{hkl}^n(\varphi)$  recorded in the detector gives the convolution of the orientation distribution (at  $\psi = 0$ ) with the instrument resolution. The intrinsic mosaicity often has an irregular shape, but for practical purposes it is usually characterized by the full width at half-maximum (FWHM) of  $W_{hkl}^n(\varphi)$  (Sears, 1997).

Fig. 6(b) shows schematically the corresponding TOF transmission experiment. The geometry of the sample and incident beam are the same as in the previous figure, but now a polychromatic neutron beam and a TOF transmission detector are used to record a peak  $W_{hkl}(\lambda)$ , as given by  $1 - T(\lambda)$ . In this case the instrument resolution becomes a strip normal to the diffraction plane. To see this, we consider a region misaligned by  $\varphi$  from the average  $[hkl]$  orientation. As the misalignment occurs in the diffraction plane, the diffraction angle changes by  $\Delta\alpha_{hkl} = \varphi$ , so neutrons of a slightly different wavelength ( $\lambda + \Delta\lambda$ ) are now removed from the beam. By contrast, when the misalignment is normal to the diffraction plane, the diffraction angle remains constant and the wavelength  $\lambda$  of the diffracted neutrons remains the same. Thus the intensity  $W_{hkl}(\lambda)$  recorded at the detector corresponds to the integral of  $W_{hkl}(\varphi, \psi)$  over all values of  $\psi$  at a fixed value of  $\varphi$ , as is shown schematically in the figure. The uncertainty in  $\varphi$ , *i.e.* the width of the strip, is defined by the collimation of the incident beam in the diffraction plane.

To estimate the combined angular uncertainty  $\Delta\alpha_{hkl}$ , we assume that the resulting distribution has a width given by the square sum of the individual distributions, *i.e.*

$$(\Delta\alpha_{hkl})^2 = \{\text{FWHM}[W_{hkl}^n(\varphi)]\}^2 + \eta_n^2, \quad (12)$$

where  $\eta_n$  is the incident-beam divergence in the diffraction plane. The reported mosaicity of the specimen is 3 min, or  $870 \mu\text{e}$ , as measured with a polychromatic  $\gamma$ -ray diffractometer (Bastie *et al.*, 2000). The evaluation of equation (12) results in values of  $\Delta\alpha_{hkl}$  of  $2701 \mu\text{e}$  and  $1875 \mu\text{e}$  for the two experiments described here, which compare very well with the experimental values of  $(2746 \pm 90) \mu\text{e}$  and  $(1733 \pm 100) \mu\text{e}$ . The relatively large deviation of the measured peak widths from the lines displayed in Fig. 5 is discussed later.

## 6. Tensile tests

As an application of this technique we have studied the plastic deformation by tensile loading of a Cu monochromator. A more comprehensive description of the problem, including the main experimental results, has been presented elsewhere (Santisteban *et al.*, 2005). Here we concentrate on those aspects showing the capabilities of this new technique.

The monochromator (100 mm long, 50 mm wide and 10 mm thick) was produced by Metal Crystals, Cambridge, UK, by hot-pressing plastic bending of a single crystal grown by the Czochralski/Bridgman method. The monochromator had the [110] crystallographic axis parallel to the normal direction (ND), the [001] axis along the transverse direction (TD) and the [110] axis along the longitudinal direction (LD), as shown in Fig. 4. The monochromator was originally designed to make

use of the [110] planes in reflection mode. A flat tensile specimen with the geometry indicated in the figure was loaded *in situ* during the experiments.

Loading was performed using a stress rig that sits horizontally on a goniometer that allows changing the angle between the tensile axis and the incident neutron beam. The specimen was loaded up to 2% linear strain through a series of predefined strain values. Fig. 7(a) shows the recorded stress-strain curve, which displays a short elastic regime followed by yield at  $\sim 25$  MPa. Fig. 7(b) shows a detail of the transmission spectra recorded at the start and end of the tensile tests. As seen in the figure, deformation affects both the position and width of the Bragg peaks observed in the transmitted beam. TOF transmission spectra were recorded at each strain value for two orientations, with the tensile axis making angles of  $62.0^\circ$  and  $63.3^\circ$  with the incident beam. Five transmission spectra were simultaneously recorded for each strain and orientation, as given by the counts recorded by five columns of the pixellated detector. This corresponds to different positions along the tensile axis of the specimen, schematically indicated

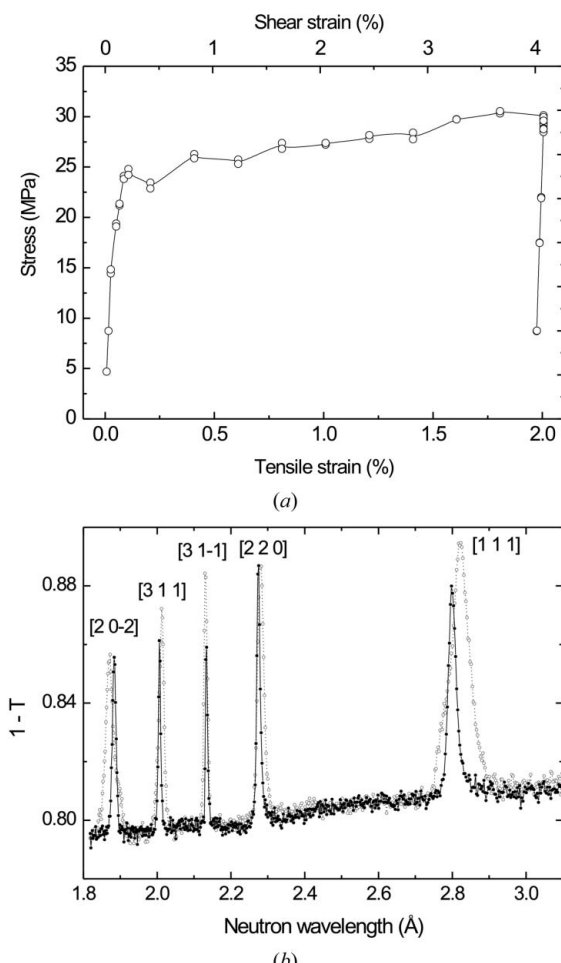


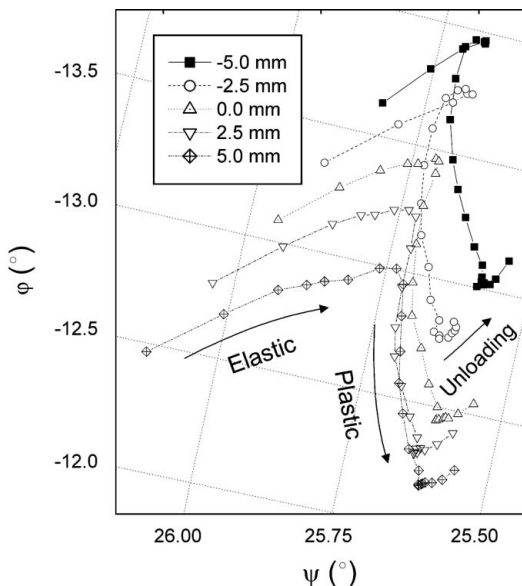
**Figure 7**

(a) Stress-strain curve of a tensile specimen loaded in tension along the [110] direction. Loading was performed in strain control mode and unloading in stress control mode. (b) Detail of the changes observed in the transmission spectrum as a result of plastic deformation. The solid circles correspond to the start of the test and the open symbols to the end.

**Table 2**

Typical parameters for the peaks used in the analysis of the tensile tests on the Cu monochromator.

Index $hkl$	Experimental position $\lambda_{hkl}^{\text{exp}}$ (Å)	Fit position $\lambda_{hkl}^{\text{fit}}$ (Å)	Difference $\lambda_{hkl}^{\text{exp}} - \lambda_{hkl}^{\text{fit}}$ ( $\mu\text{e}$ )	Gauss width $\delta\sigma_{hkl}$ ( $\mu\text{e}$ )	Angle $\alpha_{hkl}$ (°)
[200]	3.3847 (2)	3.38636	-450	1920 (60)	20.487
[111]	3.3006 (2)	3.30179	-390	2360 (60)	37.714
[111]	2.8254 (1)	2.82448	350	3450 (60)	47.376
[220]	2.29716 (6)	2.29735	-70	1800 (40)	25.961
[311]	2.13232 (5)	2.13189	180	760 (40)	11.867
[311]	2.00155 (6)	2.00172	-120	1160 (40)	23.276
[202]	1.8727 (1)	1.87217	290	2340 (60)	42.865

**Figure 8**

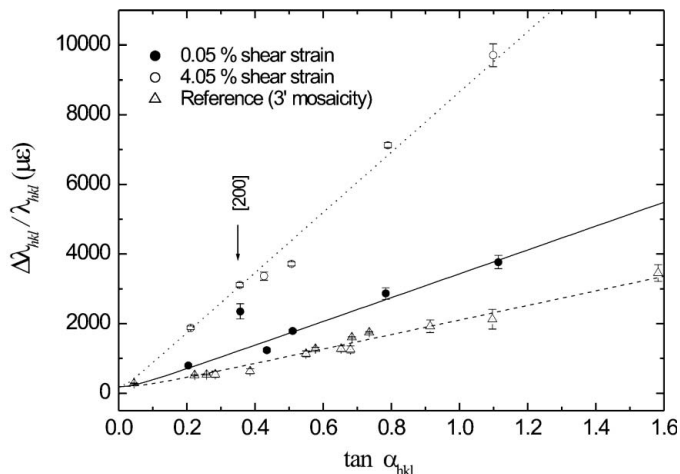
Evolution of the direction of the incident neutron beam through the tensile tests, as seen from different parts of the specimen.  $\psi$  and  $\varphi$  are the spherical angles in a system with the  $Z$  axis along the [110] and the  $X$  axis along the [110] direction. The differences between the curves represent the variation in orientation that exists in the specimen over a macroscopic scale. The error in both axes is approximately 1 min.

by the five detectors in Fig. 4. The detectors are labelled ( $-5.0$  mm), ( $-2.5$  mm), ( $0.0$  mm), ( $2.5$  mm) and ( $5.0$  mm), according to the location along LD of the corresponding gauged volume (from the middle of the specimen). A 2 mm wide strip of the sample was gauged by each detector. Counting times of 9 min per orientation were used through the experiments.

The first seven reflections, *i.e.* those appearing at longer wavelengths, were analysed to track the evolution of the orientation and mosaicity of the sample. Table 2 identifies the indexed reflections, listing typical positions and widths of the peaks. In total, 230 of such tables, corresponding to 23 loads, two orientations, and five detectors, were produced for the present analysis.

### 6.1. Crystal orientation

Fig. 8 shows the evolution of the incident-beam direction, as seen from the different volumes of the specimen sampled by each detector. The incident-beam direction is displayed in terms of the spherical angles ( $\psi, \varphi$ ) for a coordinate system

**Figure 9**

Changes in peak width induced by plastic deformation as a function of the angle  $\alpha_{hkl}$ . The solid and open circles correspond to the spectra measured at the beginning and end of the tensile tests, respectively. The triangles correspond to the peak widths of a reference specimen with a mosaicity of 3 min.

attached to the crystal lattice with the  $Z$  axis along the [110] direction and  $\varphi = 0$  for the [110] direction. The observed difference between the first points of each curve indicates that the specimen was distorted on a macroscopic scale from the onset. The differences between detectors are real, as each detector was calibrated individually with the reference sample prior to the tests. Different deformation regimes are clearly identified in the figure by sudden changes in slope, which indicates that different parts of the sample have responded to the load at different times. The graph exemplifies the angular resolution ( $\sim 1$  min) achievable by this technique. For a proper interpretation of these experiments, however, it is better to concentrate on the evolution of a more relevant crystal direction, as the incident beam was not aligned to any symmetry axis of the system. We have presented such an analysis (Santisteban *et al.*, 2005) and show that the ND rotates around an axis that is not parallel to the direction of the applied load. We also give an interpretation of the present results in terms of the interaction between the active slip systems and the constraints imposed at the specimen ends.

### 6.2. Mosaicity

Fig. 9 shows the width of the Bragg reflections measured at the beginning and at the end of the tensile tests, compared with the widths of the reference specimen measured under the

same experimental conditions. The error bars displayed in the figure correspond with the standard deviation observed across the detectors. The dependence of peak width on  $\tan \alpha_{hkl}$  is well described by equation (11), indicating that the mosaicity of the specimen is relatively isotropic throughout the tests. The angular uncertainties measured at the beginning and at the end of the tests are 3430 (300)  $\mu\text{e}$  and 8650 (450)  $\mu\text{e}$ , respectively. This is equivalent to an overall increase in the mosaicity of the crystal from 10 min to 30 min. On the other hand, a small standard deviation of interplanar distances ( $\sim 200 \mu\text{e}$ ) is observed in all detectors and for all strain values, which is compatible with the standard deviation observed in the lattice parameter ( $\sim 200 \mu\text{e}$ ) from the analysis of the peak positions.

Despite the nearly isotropic behaviour displayed by the sample, a closer examination of the data reveals that at the start of tests the mosaicity of the [200] reflection was considerably larger than the rest. However, at the end of the test the mosaicity of the [200] reflection was similar to that of the other reflections. This anisotropic response is better illustrated in Fig. 10, which shows the evolution of the mosaicity of reflections [200], [111] and [111] *versus* the equivalent shear strain and applied load. The data correspond to the average response across the specimen, with the error bars representing the associated standard deviation. In Fig. 10(a), we see that the mosaicity of reflection [200] remains almost constant until its value equals those of the other reflections. At that point, the

mosaicity of [200] starts increasing, at exactly the same rate as the [111] and [111] reflections, *i.e.* 5 min per percentage of shear strain.

On the other hand, Fig. 10(b) shows that, as expected, the mosaicity remains constant during the elastic loading and unloading of the specimen. Moreover, the changes in mosaicity of [111] and [111] reproduce quite closely the stress-strain curve presented in Fig. 7(a). The other reflections analysed showed a response very similar to [111] and [111].

A simple interpretation of these results is straightforward. Up to a load of 27 MPa, the deformation is accommodated elastically; there is a sharp reorientation of the crystal which realigns the different regions of the sample; and no change in mosaicity. After that, plastic deformation starts and there is an increase in mosaicity and a much slower reorientation rate. The low yield stress of the material is manifested in a constantly small value for the standard deviations of  $(\Delta d_{hkl}/d_{hkl})$  and lattice parameter, reflecting that the mosaic blocks change in shape and orientation with little resistance from their neighbours.

## 7. Discussion

The experiments on Cu crystals have probed the effectiveness of the technique introduced here for the determination of crystal orientation, lattice parameter, and interplanar distances from the analysis of the neutrons transmitted by mosaic crystals. In particular, the results for the reference sample presented on Table 1 have probed the validity of equation (4) to describe the positions of the dips appearing in the transmitted spectrum. However, a closer look at the table reveals that the differences between the experimental and refined peak positions are larger than the experimental errors. The difference does not present an obvious trend with respect to neutron wavelength or diffraction angle, but overall the standard deviation of the predicted positions ( $90 \mu\text{e}$ ) is clearly larger than the average experimental uncertainty in the determination of the peak position ( $25 \mu\text{e}$ ). A larger disagreement between experimental and predicted peak positions is observed for the tensile specimen, as is evident from the data listed in Table 2. This disagreement indicates the existence of a small systematic error in the present description of the experiment, raising some concern about the physical meaning of the errors in the direction cosines and lattice parameter reported from the least-squares refinement. In fact, a better figure for the actual uncertainty in the determination of the crystal orientation and lattice parameter can be drawn from the reported standard deviations between predicted and observed peak positions. A standard deviation of  $\sim 300 \mu\text{e}$  in the determination of the peak positions translates into an overall uncertainty of 1 min of arc in the crystal orientation. This value for the angular uncertainty is consistent with the typical deviation of the data presented in Fig. 8, which is still good enough to determine the rotations occurring during the first hundreds of  $\mu\text{e}$  of plastic deformation.

The cause of the disagreement is likely to be the existence of macroscopic (type I) stresses within the sample volume

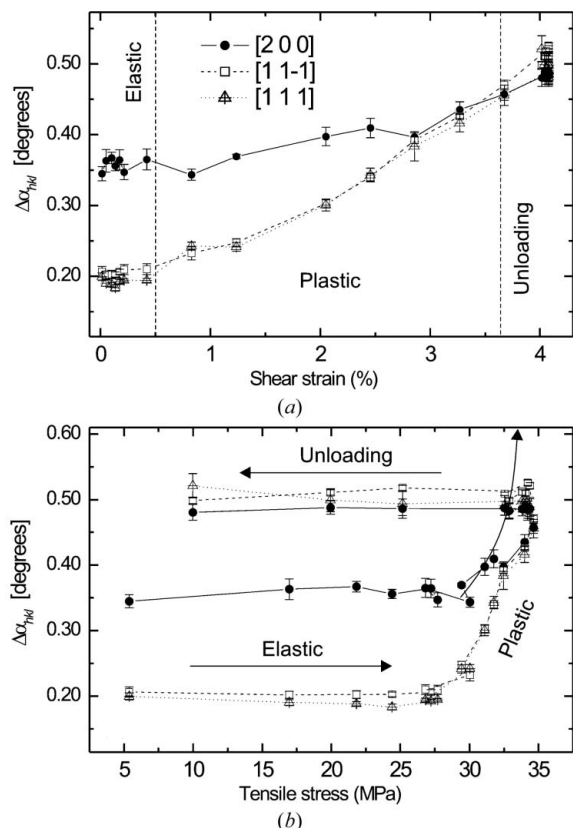


**Figure 10**

Evolution of the mosaicity of reflections 200, 111 and 111 during the tensile tests on the Cu monochromator: (a) as a function of equivalent shear strain, and (b) as a function of applied tensile stress. The deformation regimes are identified in each case.

gauged by the experiment. Such stresses result in the elastic distortion of the cubic cell, and hence a deviation of the peak positions from the wavelengths predicted by equation (4). In this sense, the average deviation of  $250 \mu\text{e}$  for the tensile specimen is compatible with the yield stress ( $\sim 27 \text{ MPa}$ ) observed in Fig. 7(a), when typical values for the single-crystal elastic constants for Cu ( $C_{11} = 168 \text{ GPa}$  or  $C_{12} = 121 \text{ GPa}$ ) are considered. Of course, in this situation a single lattice parameter is unable to reproduce all of the observed peak positions, so a less symmetric structure should be used to describe the crystal lattice. For the general case, *i.e.* when no assumptions about the principal axes of the stress tensor can be made, a triclinic structure should be adopted. However, the addition of five extra fitting parameters calls for more peaks to be included in the analysis, which is particularly difficult within the single peak fitting procedure presented here due to the inevitable peak overlap found at short wavelengths. Hence a full-pattern least-squares refinement should be considered to tackle such a problem.

Concerning the peak widths, we have shown that a quite irregular dependence of peak width on neutron wavelength can be effectively described by considering the angle between the diffraction plane normal and the incident beam. This is summarized by Fig. 5, which shows an almost linear dependence of peak width on the tangent of the angle. Moreover, we are also able to predict the observed slopes based on the crystal mosaicity of the reference sample and the values of the incident-beam divergence during the experiments. However, there is a large scatter in Fig. 5 around both lines, clearly larger than the reported error bars. The problem here lies in the intrinsic complexity of the real distributions of crystal orientations and incident neutron directions, which we have represented using simple analytical functions. Even when the experimental signal may be well described by the convolved peak profile adopted here, the fine details of the individual distributions are lost in the convolution process. We know that this is the case because the rocking curves measured on Cu mosaic crystals using  $\gamma$  rays (where the beam divergence is negligible) show complex shapes that vary strongly across the sample and between different reflections (Schneider, 1974). Consequently, the scatter observed in Fig. 5 is not unreasonable considering the comparison of the widths of 14 different reflections. On the other hand, as the error bars in Fig. 5 suggest, the sensitivity of the technique is much higher than the scatter observed around the lines. A proof of this is given in Fig. 10, which displays the evolution of the individual peak widths on plastic deformation. The error bars reported in that figure correlate well with the scatter observed for each curve, as the distributions of crystal orientations do not suffer dramatic changes after each increase in the applied strain.

During the data analysis we found that overlapping peaks prevent a sound definition of the widths for many reflections. Again, the number of useful reflections contributing to the definition of the overall mosaicity of the sample can be greatly increased by adopting the full-pattern refinement mentioned in the previous paragraph.

## 8. Conclusions

A method has been proposed to determine the orientation, mosaicity and lattice parameter of a mosaic crystal based on the analysis of the neutrons transmitted by a sample. Basically, a detector is located on a white neutron beam from a pulsed neutron source, and the reduction in beam intensity brought about by the insertion of the sample is energy-resolved with the time-of-flight technique. The transmitted neutron spectrum of a mosaic crystal presents a series of dips in intensity at specific neutron wavelengths, as a result of reflection from the crystal planes. The positions of those dips depend on the crystal structure of the material and on the orientation of the specimen. The shifts in the positions of those dips after the sample is tilted by  $1^\circ$  are exploited for the definition of the crystal orientation with a resolution of 1 min of arc. The dependence of the widths of the dips on Bragg diffraction angle provides a value for the mosaicity of the sample.

As an application of the technique, we have tracked *in situ* the evolution of crystal orientation and mosaicity of a Cu monochromator plastically deformed by uniaxial tension along the [110] direction. Several locations of the specimen were studied simultaneously, showing differences in the evolution of the crystal orientation across the specimen. An initially anisotropic mosaicity became more isotropic as a result of the plastic deformation. On average, a linear increase of mosaicity at a rate of  $\sim 5$  min per percentage of shear strain was observed.

The technique is available on the ENGIN-X beamline at the Isis Facility, Rutherford Laboratory, UK. In its present state, it can produce maps of the macroscopic distribution of crystal orientation and mosaicity for several reflections simultaneously with a spatial resolution of  $2 \times 2 \text{ mm}$ . The development of a new generation of neutron spallation sources providing a tenfold increase in neutron intensity suggests that full orientation and mosaicity mapping on a macroscopic scale will be available in the near future.

## APPENDIX A

### Indexing of the peaks observed in TOF transmission

The first step in the analysis of the transmitted TOF spectrum is the indexing of the peaks. In order to do so, we start by creating a list ( $\lambda_1 > \lambda_2 > \dots > \lambda_N$ ) with the experimental positions of the first  $N$  peaks, *i.e.* those observed at longer wavelengths. We note that according to equation (5) the maximum wavelength at which a reflection belonging to the  $\langle hkl \rangle$  family can appear is

$$\lambda_{hkl}^{\max} = 2d_{hkl}. \quad (13)$$

At this wavelength the diffracting planes are perpendicular to the incident neutron beam (in polycrystalline materials, this condition results in the appearance of the so-called Bragg edges in the transmitted spectrum). We compile a list with the maximum wavelength for each crystal family ( $\lambda_I^{\max}, \lambda_{II}^{\max}, \dots$ ), where the family has been identified by a Roman numeral in descending order of  $d_{hkl}$ . We note the following.

(i) No peaks should be observed for wavelengths longer than  $\lambda_1^{\max}$ .

(ii) For wavelengths  $\lambda > \lambda_{\text{II}}^{\max}$ , only peaks originated from reflections from the first crystal family are observed. For wavelengths  $\lambda > \lambda_{\text{III}}^{\max}$ , only peaks from the first and second crystal families are allowed; and so on.

(iii) The smallest peak position considered for the analysis,  $\lambda_N$ , defines the highest crystal family index to be considered in the indexing process.

With this information we realise that if a peak is observed at a wavelength longer than  $\lambda_{\text{II}}^{\max}$  it can be unambiguously identified as belonging to the first crystal family. The choice of the actual indexes  $[h_0k_0l_0]$  for this first reflection will be arbitrary, as all reflections in the family are equivalent. The wavelength  $\lambda_{h_0k_0l_0}$  at which this peak is observed also tells us the angle  $\alpha_{h_0k_0l_0}$  between  $[h_0k_0l_0]$  and the incident beam. So our only uncertainty now is the actual rotation of the crystal around the incident beam. This problem can be easily resolved in the coordinate system of the crystal, where the possible orientations of the incident beam will lie in a cone of axis  $[h_0k_0l_0]$  and semi angle  $\alpha_{h_0k_0l_0}$ . The coordinates of the points lying in the intersection of this cone with the unit sphere can be parameterized in terms of a single variable, *i.e.*  $[x(\varphi), y(\varphi), z(\varphi)]$ . For each value of  $\varphi$ , the positions  $\lambda_{hkl}$  for all allowed reflections are calculated, and the  $N$  largest values are compared with the experimental values ( $\lambda_1 > \lambda_2 > \dots > \lambda_N$ ). As only one degree of freedom is involved, the indexation is now transformed into a simple one-variable least-squares minimization problem. The output from this process are the coordinates ( $x, y, z$ ) and the  $hkl$  indexes for the first  $N$  reflections at  $\varphi = \varphi_{\min}$ . Provided with this information, the precise orientation of the incident beam can be achieved by the least-squares minimization of equation (4) as described in §4.1.

When no peak is observed at wavelengths larger than  $\lambda_{\text{II}}^{\max}$ , the situation is slightly more complicated. If the first peak is observed at a wavelength  $\lambda_1$  longer than  $\lambda_{\text{III}}^{\max}$ , then it can belong to either the first or second crystal family. In such a case, both possibilities should be considered using the procedure proposed above. Only one of the options is capable of describing the observed peak positions.

The author wishes to thank Mike Hutchings and Pierre Courtois for kindly providing and characterizing the crystals

used in this work; Pete Ledgard for producing the tensile specimens, Mark Daymond, Lucia Alianelli, Ed Oliver and Vadim Stelmukh for their help during the experiments; Lyndon Edwards for fruitful discussions, and Robert Dalglish for assistance with the Monte Carlo simulations.

## References

- Alianelli, L. (2002). PhD Thesis, University Joseph Fourier, France.  
 Bastie, P., Hamelin, B. & Courtois, P. (2000). *J. Phys. IV France*, **10**, 10–21.  
 Bunge, H. J. (1982). *Texture Analysis in Materials Science*. London: Butterworths.  
 Courtois, P., Berneron, M., Escoffier, A., Hamelin, B., Hehn, R., Hetzler, E., Menthonnex, C. & Mestrallet, B. (2002). *ILL Annual Report*, available online at [http://www.ill.fr/AR-02/site/areport/fset\\_96.htm](http://www.ill.fr/AR-02/site/areport/fset_96.htm).  
 Dann, J. A., Daymond, M. R., Edwards, L., James, J. & Santisteban, J. R. (2004). *Physica B*, **350**, 511–514.  
 Freund, A. K. (1983). *Nucl. Instrum. Methods*, **213**, 495–501.  
 Frey, F. (1974). *Nucl. Instrum. Methods*, **124**, 93–99.  
 Granada, J. R. (1984). *Z. Naturforsch. A*, **39**, 1160–1167.  
 Ikeda, S. & Carpenter, J. M. (1985). *Nucl. Instrum. Methods A*, **239**, 536–544.  
 Kashihara, K., Tagami, M. & Inoko, F. (1996). *Mater. Trans. JIM*, **37**, 564–571.  
 Kropff, F., Granada, J. R. & Mayer, R. E. (1982). *Nucl. Instrum. Methods*, **198**, 515–521.  
 Naguib, K. & Adib, M. (1996). *J. Phys. D Appl. Phys.*, **29**, 1441–1445.  
 Nielsen, K. & Lefmann, K. (2000). *Physica B*, **283**, 426–432.  
 O'Connor, D. A. & Sosnowski, J. (1961). *Acta Cryst.* **14**, 292–297.  
 Santisteban, J. R., Edwards, L., Fitzpatrick, M. E., Steuwer, A., Withers, P. J., Daymond, M. R., Johnson, M. W., Rhodes, N. & Schooneveld, E. M. (2002). *Nucl. Instrum. Methods A*, **481**, 255–258.  
 Santisteban, J. R., Oliver, E. C., Daymond, M. R., Alianelli, L. & Edwards, L. (2005). *Mater. Sci. Eng. A*. In the press.  
 Santisteban, J. R., Steuwer, A., Edwards, L. & Withers, P. J. (2001). *J. Appl. Cryst.* **34**, 289–297.  
 Santisteban, J. R., Steuwer, A., Edwards, L., Withers, P. J. & Fitzpatrick, M. E. (2002). *J. Appl. Cryst.* **35**, 497–504.  
 Schneider, J. R. (1974). *J. Appl. Cryst.* **7**, 541–546.  
 Sears, V. F. (1997). *Acta Cryst. A*, **53**, 35–54.  
 Wert, J. A. & Huang, X. (2003). *Philos. Mag.* **83**, 969–983.  
 Wert, J. A. (2004) *Proceedings of the 25th Risø International Symposium on Materials Science: Evolution of Deformation Microstructures in Three-Dimensions*, pp. 187–210. Risø National Laboratory, Roskilde, Denmark.